MATERIALS SCIENCE

Strain tolerance of two-dimensional crystal growth on curved surfaces

Kai Wang[1]*, Alexander A. Puretzky[1], Zhili Hu[2], Bernadeta R. Srijanto[1], Xufan Li[1], Nitant Gupta[3], Henry Yu[3], Mengkun Tian[4], Masoud Mahjouri-Samani[1†], Xiang Gao[5], Akinola Oyedele[1], Christopher M. Rouleau[1], Gyula Eres[5], Boris I. Yakobson[3], Mina Yoon[1], Kai Xiao[1]*, David B. Geohegan[1]*

Two-dimensional (2D) crystal growth over substrate features is fundamentally guided by the Gauss-Bonnet theorem, which mandates that rigid, planar crystals cannot conform to surfaces with nonzero Gaussian curvature. Here, we reveal how topographic curvature of lithographically designed substrate features govern the strain and growth dynamics of triangular WS_2 monolayer single crystals. Single crystals grow conformally without strain over deep trenches and other features with zero Gaussian curvature; however, features with nonzero Gaussian curvature can easily impart sufficient strain to initiate grain boundaries and fractured growth in different directions. Within a strain-tolerant regime, however, triangular single crystals can accommodate considerable (<1.1%) localized strain exerted by surface features that shift the bandgap up to 150 meV. Within this regime, the crystal growth accelerates in specific directions, which we describe using a growth model. These results present a previously unexplored strategy to strain-engineer the growth directions and optoelectronic properties of 2D crystals.

INTRODUCTION

One of the most attractive properties of emerging two-dimensional (2D) materials is their mechanical compliance, which can exceed that of their bulk counterparts by two orders of magnitude (*1*, *2*). Their strain tolerance is being exploited to explore strain engineering of their properties for new applications (*1*–*3*), including bandgap tuning for energy harvesting, funneling of excitons (*4*, *5*) and localization of single photon emission sites for quantum information science (*6*, *7*), and control of phonon bandgaps affecting thermal and mechanical properties (*8*). One method to impose localized strain in 2D crystals is to use the out-of-plane curvature of lithographically patterned features to stamp 2D crystals that have been transferred onto flexible substrates. However, this method tends to result in nonuniform strain from wrinkles and cracks, as well as unavoidable polymer residues (*1*, *9*). Instead, it would be highly advantageous to engineer the curvature of topologically patterned surfaces to locally induce strain directly during the growth of 2D crystals. Fundamental studies to determine the conformal growth capabilities of 2D crystals, the limits of their strain tolerance, and the effects of surface curvature on their growth mechanisms and dynamics (*3*, *10*–*12*) have not been carried out to date yet are essential for the 3D integration of atomically thin 2D crystals and may ultimately limit or alter attempts for scalable, large-area growth on practical substrates.

Here, we reveal the effects of strain on the vapor transport growth and optical properties of monolayer (ML) WS_2 crystals on SiO_2 surfaces induced by lithographically patterned features with both zero and nonzero Gaussian curvatures. The direct bandgap (*13*) and superior elastic strain limit (*14*) of these ML transition metal dichalcogenide (TMDC) crystals make them an ideal platform to explore this interplay between growth dynamics and curvature-induced strain. Photoluminescence (PL), Raman scattering, and second harmonic generation (SHG) are used as sensitive spectroscopic diagnostic measures of bandgap shifts, strain, and crystal orientation, respectively (*15*). Increasing tensile strain shrinks the bandgap (red shift in PL) before a direct-to-indirect gap transition takes place, while compressive strain generally increases the bandgap (blue shift in PL) (*1*, *16*, *17*). For phonons, tensile strain usually results in a softening of phonon modes revealed by Raman spectroscopy (*11*), while compressive strain results in a stiffening of modes.

RESULTS

Lithographically patterned surface features of various geometries with Gaussian curvatures (K_G), from zero to negative/positive values, including trenches and donuts of different heights, were designed and patterned on SiO_2/Si substrates, as shown in Fig. 1, A and B (see also fig. S1). Linear steps as in Fig. 1A have zero K_G and do not require a crystal to stretch to conform, so, here, we focus on the donut as a model surface, as it is a common geometry containing regions of both positive and negative curvature (Fig. 1C). From symmetry arguments, one can show that elasticity in a freestanding 2D TMDC crystal, within the linear regime, is isotropic (*18*, *19*); hence, any elastic deformations within the sheet imposed by surface curvature can be readily described theoretically by the second Föppl–von Kármán equation (see section S1) (*18*). To give an example of the predicted strain distribution in a 2D crystal conforming to a donut surface, we calculated an ML MoS_2 conformally adhering to a 40-nm donut using the Stillinger-Weber potential to model the elastic properties and a continuum elasticity model to include an applied external force field that mimics the adhesive interaction with the substrate (see section S1 and fig. S2). The results show that portion of the crystal inside the donut incurs the most (tensile) strain and that strain distribution is spatially symmetric (Fig. 1D). In addition, throughout our experiments, we measure strain distribution from the PL peak shifts (which gives

[1]Center for Nanophase Materials Sciences, Oak Ridge National Laboratory, Oak Ridge, TN 37831, USA. [2]College of Aerospace Engineering, Nanjing University of Aeronautics and Astronautics, 29 Yudao Street, Nanjing 210016, China. [3]Department of Materials Science and NanoEngineering, Rice University, Houston, TX 77005, USA. [4]Department of Materials Science and Engineering, University of Tennessee, Knoxville, TN 37996, USA. [5]Materials Science and Technology Division, Oak Ridge National Laboratory, Oak Ridge, TN 37831, USA.
*Corresponding author. Email: wangk@ornl.gov (K.W.); xiaok@ornl.gov (K.X.); geohegandb@ornl.gov (D.B.G.)
†Present address: Department of Electrical and Computer Engineering, Auburn University, Auburn, AL 36849, USA.

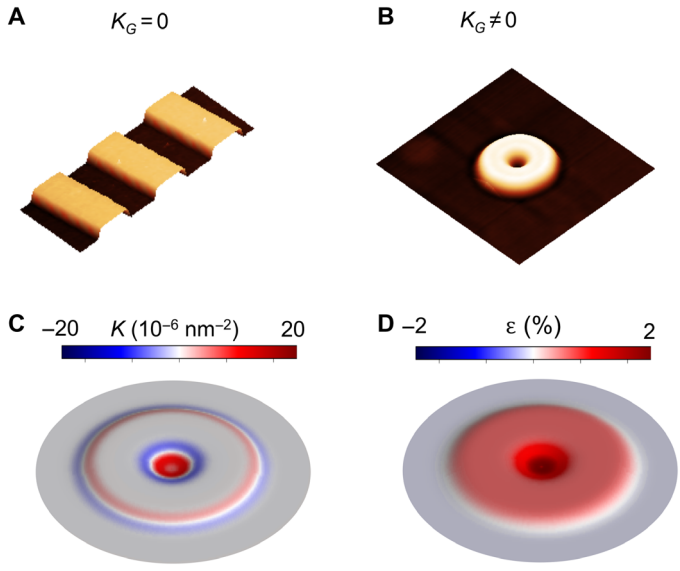

Fig. 1. Model systems with zero and nonzero Gaussian curvature to explore conformal growth of 2D crystals. (**A** and **B**) Representative atomic force microscopy (AFM) images of patterned 2-μm-wide and 40-nm-deep trenches spaced 2 μm apart with zero Gaussian curvature (K_G = 0) and 2-μm–outer diameter by 40-nm-height donuts with nonzero Gaussian curvature ($K_G \neq 0$) fabricated by etching into SiO_2 substrates. (**C**) Calculated regions of positive and negative Gaussian curvatures for a simulated 40-nm donut. (**D**) Biaxial strain profile for an ML MoS_2 crystal that conforms to a 40-nm donut calculated by the continuum elasticity model.

the bandgap shifts). Theoretical analysis shows that, because of its symmetry, the hydrostatic strain of WS_2 is proportionally related to the bandgap shift (more description given in section S1).

Strain-tolerant growth

In this study, photolithography patterned 2-μm-diameter donuts on hexagonally spaced 4-μm centers and substrate features with different curvature were fabricated to three different heights, namely, 20, 40, and 180 nm by etching the SiO_2 layer (see fig. S1). 2D flakes grown by chemical vapor deposition (CVD) on SiO_2/Si substrates always incur a global tensile strain during cooling from the growth temperature due to a thermal expansion coefficient mismatch with the substrate. For example, the tensile strain resulting from our typical growth conditions was estimated spectroscopically to be 0.4%, as calculated from a bandgap modulation of 135 meV for each percent of biaxial tensile strain (*20*, *21*) (see also fig. S3). Strain due to surface curvature was investigated using atomic force microscopy (AFM) and optical spectroscopy, which we first performed on ML WS_2 crystals that conformed to trenches as shown in Fig. 2 with different depths up to 180 nm. These structures have $K_G = 0$, yet for all trench depths (also see fig. S4), the growth was conformal, as no wrinkles, folds, or suspended layers were identified. In terms of strain distribution, Fig. 2 (E and F) shows spatial maps of PL intensity and excitonic peak position for WS_2 crystals grown on a planar SiO_2/Si substrate. Apart from the three typical dark minima tracing the progression of the corners of the crystal in the PL intensity map, the whole crystal shows a relatively uniform distribution of PL intensity and excitonic peak position. Exciton quenching at the dark minima is attributed to sulfur deficiency (*22*), but aside from this influencing the PL intensity, we also observe a SiO_2 thickness-induced interference effect (*23*), which is confirmed from the parts of a WS_2 crystal grown outside a trench exhibiting a considerably higher PL intensity than parts inside the trenches (Fig. 2I). The PL peak position corresponding to the A exciton of ML WS_2 remains essentially constant across the whole crystal (Fig. 2, G and H). In addition, the small variation in PL peak position suggests that no additional strain is built into the crystal during the growth. This latter conclusion is echoed in Fig. 2J, i.e., no peak shifts are noted in any of the prominent ML WS_2 Raman modes located at 347.0, 356.2, and 417.4 cm^{-1} (*24*). Note that this holds true for crystals grown on trenches that are 20 and 180 nm deep (20-nm case in fig. S4), indicating conclusively that these surfaces with K_G = 0 impart no additional strain to the growing WS_2 MLs. Although affected by the thickness of SiO_2 underneath the crystal, the SHG signal shows a relatively homogeneous distribution of intensity on (off) the trenches, indicative of the single crystallinity of the flake conformally grown on the trenches (fig. S4, G and H). We also checked the ML WS_2 crystal conforming to the 180-nm trenches and similarly found that no additional tensile strain was built in the crystal besides the intrinsic global tensile strain.

However, growth on arrays of patterned donuts with similar heights, where $K_G \neq 0$, induced strain and altered the growth dynamics. As shown in Fig. 3A, large ML WS_2 crystals with edge lengths from 5 to 120 μm were able to conformally coat arrays of short, 20-nm donuts, accommodating the induced strain, while retaining their equilateral-triangle shape. AFM line profiles, as shown in Fig. 3B, confirmed the conformal growth by reproducing the dimensions of the underlying donut (height, 20 nm). As shown in Fig. 3F, optical spectroscopy using the intensity of light induced by SHG was used to provide a map of the WS_2 ML, indicating that the entire crystal in the flat regions of the substrate appears to have the same crystalline orientation.

We used shifts in the PL and Raman spectra of the WS_2 crystals to estimate the strain in the crystal, which, in this case, was highly localized at the donut locations, as shown in Fig. 3. As shown in Fig. 3E, for five of the donuts highlighted in Fig. 3A, the curvature-induced strain was clearly evident and reproducible from shifts in the PL peak position. On the basis of the PL peak maps and positions such as in Fig. 3G, the WS_2 crystals are most strained inside the donut center (A), less strained on the donut body (B), and least strained outside the donuts (C). The PL red shift of 30 meV indicates that the 20-nm features generated a local biaxial tensile strain in the crystal of 0.2% from inside (A) to outside (C) the donut, which agrees quantitatively with the strain profile calculated by the continuum elasticity model (see fig. S2). This same strain was also estimated from the measured 0.8-cm^{-1} red shift in the $E_{1g}(\Gamma)$ and $A_{1g}(\Gamma)$ Raman bands from position A to position C, as shown in Fig. 3H. The strain exerted by the features appears symmetric, matching theory and calculations; however, the PL intensity map (Fig. 3D) shows an asymmetrical distribution with higher intensity at the donut edges compared to their centers. This is currently unexplained, but may arise from a combination of effects, including an artifact from optical interference due to the thickness variation of the oxide (*23*), strain-induced exciton funneling (*1*, *25*), or some heterogeneity in the crystal along the growth direction (*26*).

To confirm the curvature-induced strain in the WS_2 ML, we detached the crystals from the patterned substrates and transferred them to a flat SiO_2/Si substrate (fig. S5). Spatial PL maps (fig. S5) revealed no PL shifts, indicating that both the intrinsic global biaxial strain and the curvature-induced local strain within the WS_2 ML crystals are released after removing the patterned substrate. Moreover, further scanning transmission electron microscopy (STEM) imaging, as

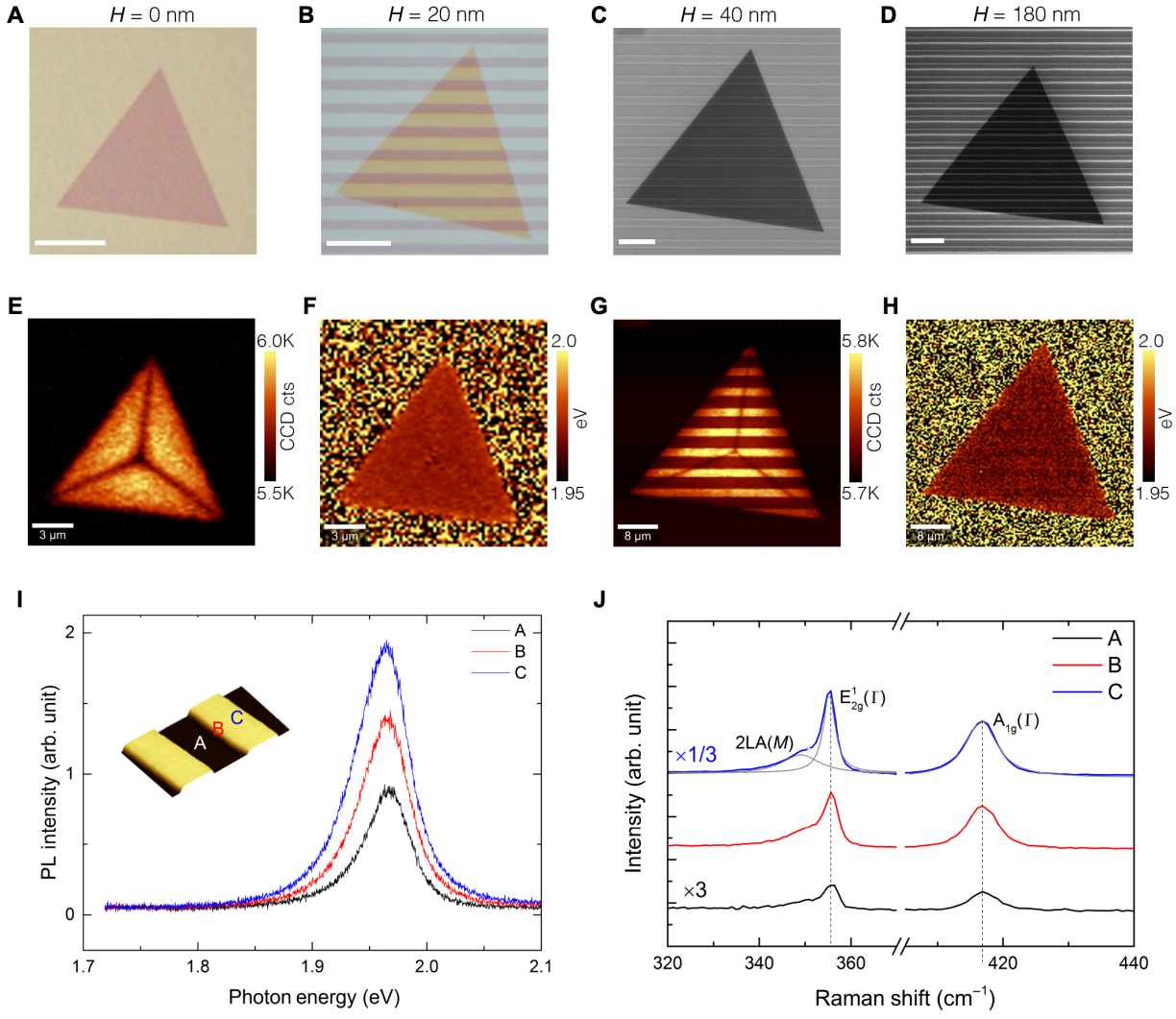

Fig. 2. ML WS_2 crystals grown on substrate surfaces with $K_G = 0$. (**A** to **D**) Crystal morphologies for an individual ML WS_2 flake grown on flat SiO_2/Si substrates (A) and patterned trenches with a height (*H*) of 20 nm (B), 40 nm (C), and 180 nm (D). (A) and (B) are optical micrographs, while (C) and (D) are scanning electron microscopy (SEM) images. Scale bars, 5 μm. (**E** and **F**) Spatial maps of PL intensity and peak position of an individual WS_2 flake on a SiO_2/Si flat substrate in (A). CCD, charge-coupled device; cts, counts. (**G** and **H**) Spatial maps of PL intensity and peak position of an individual WS_2 flake on the 40-nm patterned trenches in (C). (**I** and **J**) PL and Raman spectra obtained from three different spots, A, B, and C. Inset in (I): 3D AFM height profile illustrates the location of A (on the trench), C (off the trench), and B (in between). All the optical data were acquired with a 488-nm laser. arb. unit, arbitrary unit.

shown in fig. S5, also revealed that no freestanding donut-shaped features of WS_2 were discernible, indicating that the stretched crystals that conformed to the donuts had no observable residual deformation after the strain was released.

Crystal branching and nonlocal strain distribution

Growth of ML WS_2 on taller 40-nm donuts with higher local curvature resulted in strain-tolerant growth of triangular WS_2 ML crystals displaying both continuous edges and branched triangles with jagged edges, as shown in scanning electron microscopy (SEM) images in Fig. 4 (A to C). Again, spatial maps of PL intensity (Fig. 4, D to F) revealed that the part of the WS_2 crystal on the donut showed stronger PL intensity than that outside. In addition, all three flakes showed typical minima in PL intensity that follow the evolution of the crystal corners and can be traced back to their intersection to locate the crystal nucleation point in the spatial map. Note that both triangular flakes in Fig. 4 (D and E) are not centrosymmetric. This will be elaborated in the following section. Two of the three minima in the branched triangle shown in Fig. 4E intersect donuts, indicating that crystal branching appears favorable when two edges encounter a donut during growth.

First, the PL peak position maps shown in Fig. 4 (G to I) reveal localized strain as an optical bandgap decrease in the crystals not only on the donut feature but also in extended areas adjacent to them along the normal to the direction of crystal growth (symmetrical dark area in Fig. 4G). Second, continuing outward along this growth direction, a bright area right after the donut indicates that a region of compressive strain occurs in the crystal. Third, when branching occurs, an asymmetrical tensile strain distribution appears right after the donut (Fig. 4H). This indicates that the strain distribution of a crystal grown on these donuts can be nonlocal, which is distinct from the localized strain distribution that was observed in crystals on 20-nm

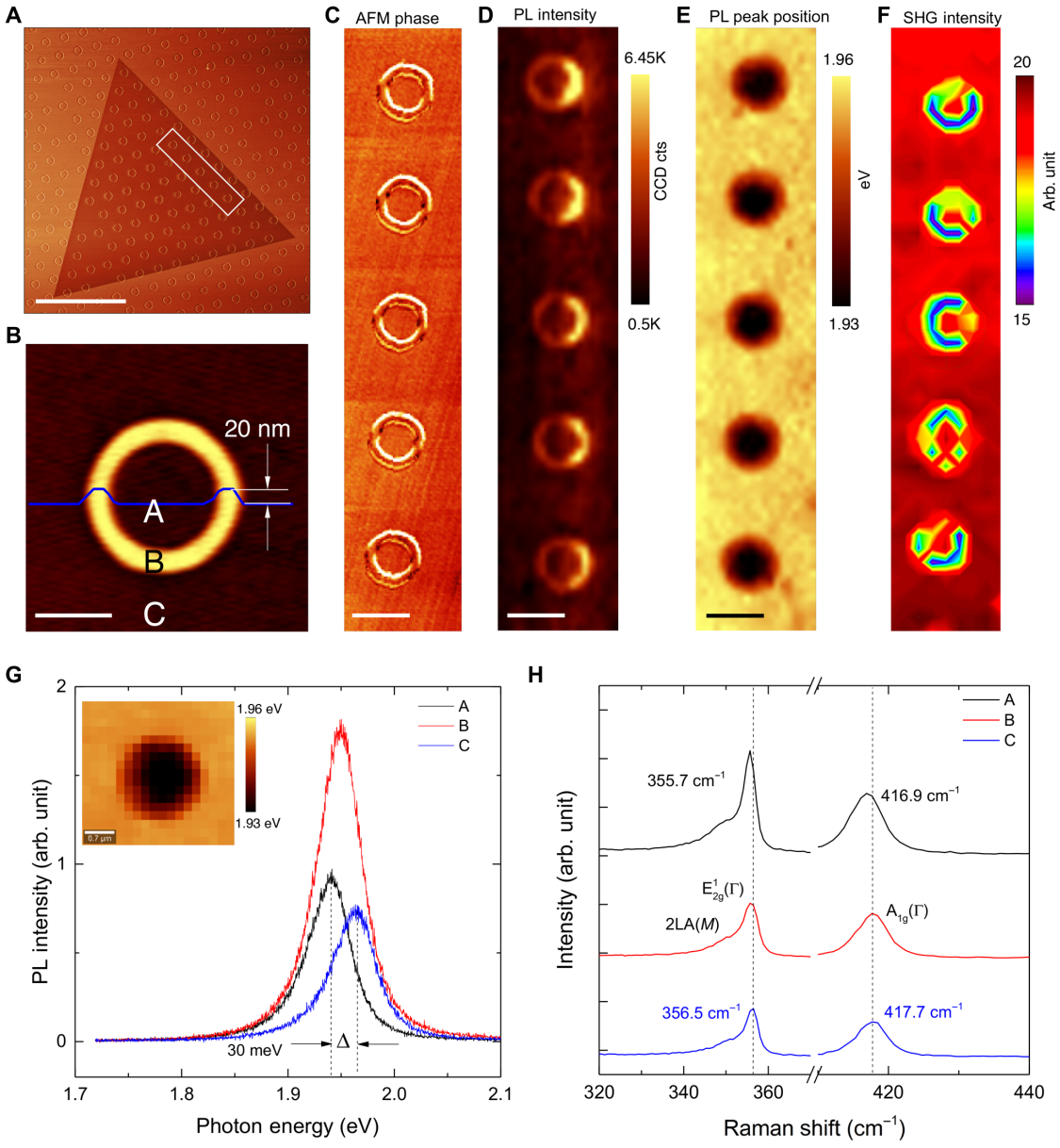

Fig. 3. Strain-tolerant growth of ML WS_2 crystal on an array of 20-nm donuts. (**A**) AFM phase image (scale bar, 20 μm) of a triangular ML WS_2 crystal grown on a hexagonal array of 1.7-μm-diameter, 20-nm-height donuts on 4-μm centers. (**B**) AFM image (scale bar, 1 μm) taken from an individual donut with the corresponding AFM height profile (inset blue curve). (**C**) AFM phase image and spatial maps of (**D**) PL intensity, (**E**) PL peak position, and (**F**) SHG intensity (scale bars, 2 μm) corresponding to the highlighted region in (A). The PL intensity was integrated from 1.85 to 2.18 eV, and the SHG intensity was integrated from 370 to 400 nm. (**G**) PL spectra of ML WS_2 crystal taken from the center (A), the body (B), and outside the donut (C), as shown in (B), revealing a $\Delta = 30$ meV peak shift from A to C. The inset shows a high-resolution spatial map of PL peak position for the WS_2 ML crystal grown on an individual 20-nm donut, indicating spatially symmetric curvature-induced strain. (**H**) Raman spectra taken from the A, B, and C points of the covered donut and corresponding 0.8-cm^{-1} shift in both $E_{1g}(\Gamma)$ and $A_{1g}(\Gamma)$ modes from A to C.

donuts and "artificial atoms" in strained MoS_2 ML crystals created by a transfer approach (*11*). This also contrasts to our previous continuum elasticity analysis (Fig. 1D). The asymmetric strain profile is related to how the crystal edge propagates over the donut and can only be understood if the growth trajectory for crystal segments grown inside and outside the donut experiences different displacements during growth, as indicated by theoretical analysis of the strain distribution by molecular dynamics (MD) simulation (fig. S6). As shown in Fig. 4J, the PL spectrum (C) taken at the center of the donut shows two PL peaks, which, given the submicrometer size of the laser spot, suggests that two strained regions were probed by the laser beam. Comparing the PL spectra taken outside the donut with the one under the most tensile strain indicates a red shift of 150 meV (Δ_1 in Fig. 4J), corresponding to an additional curvature-induced tensile strain of 1.1% notwithstanding any global thermally induced strain that might exist. Corresponding Raman spectra taken from these same spots confirmed the same level of strain (see also fig. S7). The asymmetrical tensile strain distribution along the growth direction

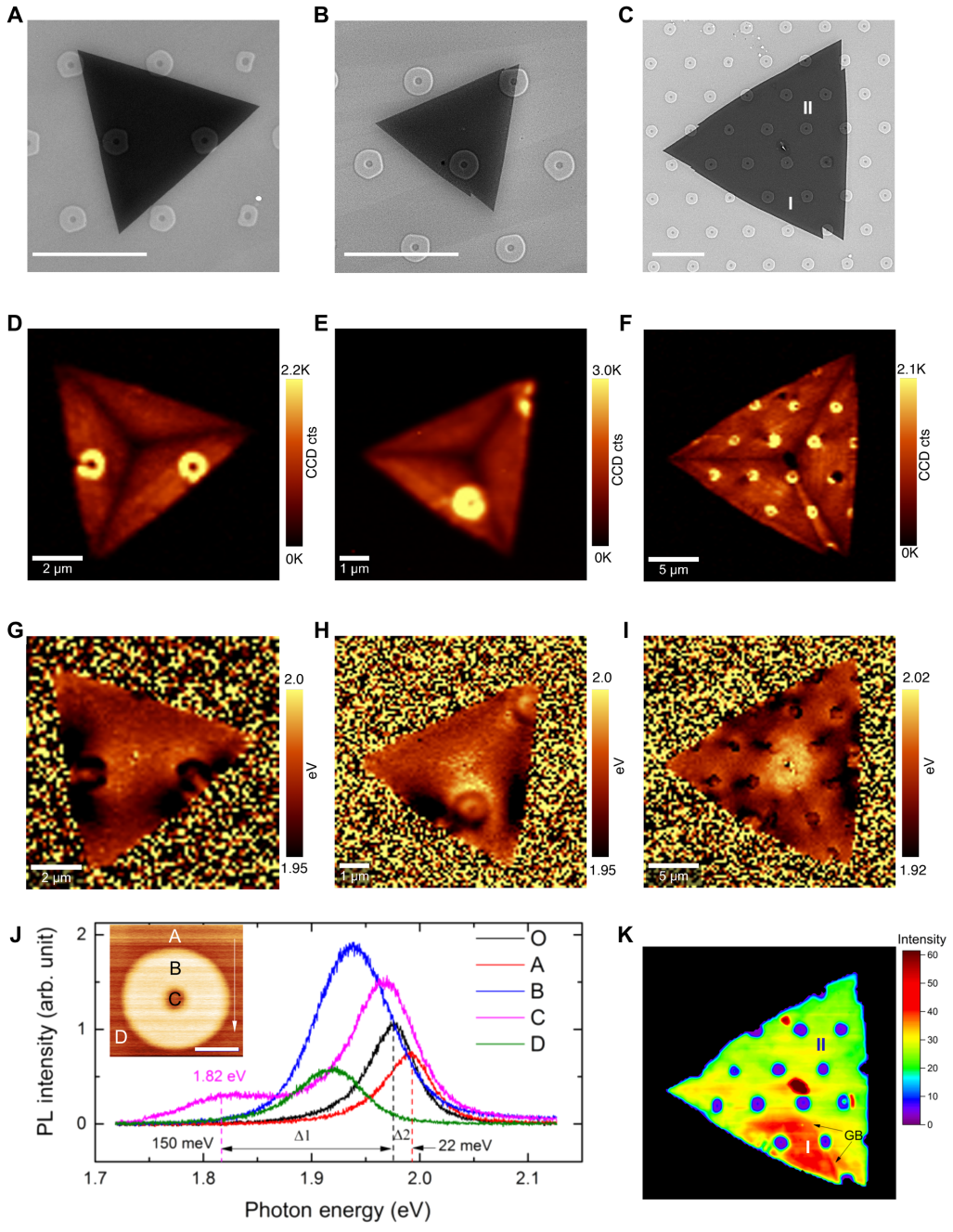

Fig. 4. Strain delocalization and evolution of crystal branching in 2D crystal growth on 40-nm donuts. (**A** to **C**) SEM images of WS_2 ML crystals (scale bars, 5 μm) grown over 40-nm-height donut structures, showing both (A) continuous and (B and C) jagged edges. Points I and II in (C) label two spots for SHG analysis in (K) revealing the onset of crystal branching seen by different crystal orientations. Corresponding spatial maps of (**D** to **F**) the PL intensity for the WS_2 crystals shown in (A) to (C). Note that the dark minima in the PL that trace the crystal corners are not centrosymmetric. (**G** to **I**) Corresponding PL peak position maps show bright (compressive) and dark (tensile) regions of strain. (**J**) PL spectra taken from the part of the WS_2 crystal that conforms to the center and edge of a donut in (G), the neighboring flat substrate, and the neighboring strained area. Inset: AFM image showing the spots A, B, C, and D for PL spectra acquisition. Spectrum O is taken from WS_2 crystal grown on flat substrate with the same crystal far from the donut, revealing a bandgap shift of $\Delta_1 = 150$ meV due to tensile strain (spectra O versus C) and $\Delta_2 = 22$ meV due to compressive strain (spectra O versus A). The white arrow illustrates the outward propagation direction of the crystal edge. (**K**) Spatial map of SHG intensity integrated from 370 to 440 nm for the flake shown in (C) reveals that crystal orientation changes only occurred in the region where branching was observed.

when crystal branching appears (Fig. 4H) indicates relaxation due to the formation of grain boundaries (GBs). As shown in Fig. 4K, we used SHG mapping and analysis to probe the crystal in Fig. 4C, and a misorientation of 3.2° was found between the two domains labeled I and II (see also fig. S7). We also performed growth on 60-nm donuts and found reproducible crystal branching (fig. S8, A and B), as we observed for taller structures, such as 180-nm donut features. Therefore, we conclude that the strain induced from the 40-nm donuts is the

threshold beyond which strain-tolerant growth transitions to crystal branching growth.

Multiple crystal domain growth

As shown in SEM images in Fig. 5 (A to D), attempting to exert much higher strains in the crystal by growing on 180-nm donuts invariably leads to the growth of multiple crystal domains. Here, we focus on flakes that nucleated in the interstitial regions between donuts and whose growth fronts, and not tips, engage an adjacent donut [other scenarios in fig. S8 (D to G)]. Qualitatively, the growth front of the crystal first approaches the donut and then starts to climb the feature (Fig. 5A). Because of the large strain induced by the curvature, the crystal growth front then breaks and splits into two or more fronts (Fig. 5B). As the growth continues, new growth fronts propagate and coalesce, giving rise to the formation of crystal GBs (Fig. 5C). The number of crystal domains multiplies as these new growth fronts encounter more donuts (Fig. 5D). As shown in Fig. 5 (F and G), the GBs between crystal domains in Fig. 5E can be identified by SHG mapping. The results suggest that by designing substrate topographies with tailored surface curvature, 2D crystals with desired misfit angle GB geometries might be realizable, as recently predicted theoretically (*27*). PL peak position maps (Fig. 5I) and spectra measured at the selected spots (Fig. 5J) revealed that the area with the most tensile strain (B) was at the donut edge, showing a 90-meV red shift (corresponding to a tensile strain of 0.7%) when compared to the unstrained area (A). Compared to the crystals that tolerated growth over 40-nm-high donuts, this somewhat lower tensile strain indicates a partial relaxation of the crystal upon GB formation. The double peaks shown in the PL spectra taken at the center (C) again suggest that

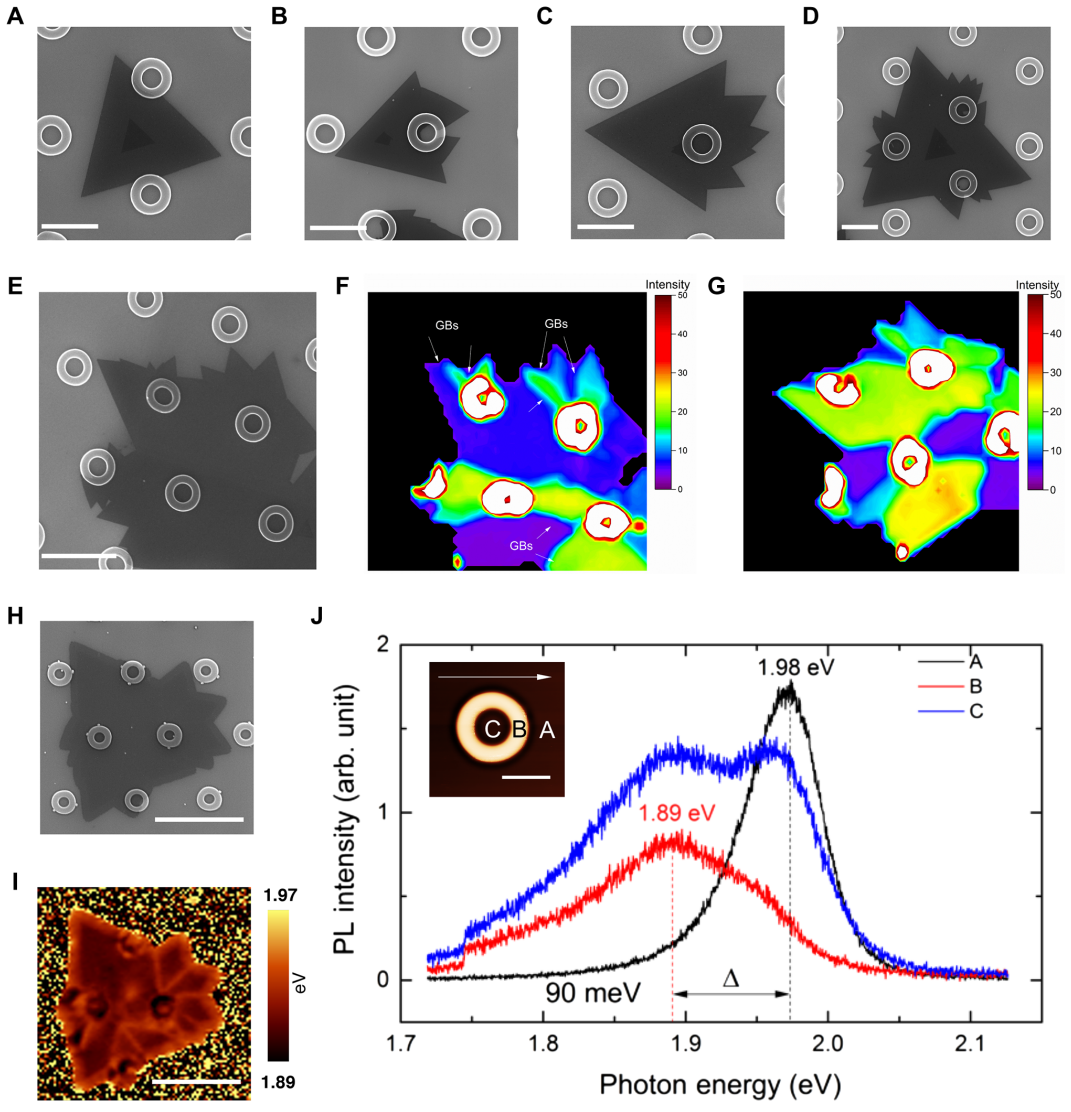

Fig. 5. Multiple crystal domain growth of 2D crystals conformed on 180-nm donut patterns. (**A** to **D**) SEM images (scale bars, 2 μm) indicating the strain-intolerant growth and formation of multiple crystal domains for WS_2 crystals encountering 180-nm-height features. (**E**) SEM image and (**F** and **G**) spatial maps of SHG intensity of the same WS_2 flake to reveal regions of different crystal orientation [image (G) was obtained by rotating the sample 30° with respect to (F)]. The high SHG intensity in the white regions was intentionally truncated. (**H** and **I**) SEM and corresponding spatial map of the PL peak position for an individual WS_2 crystal show bandgap shifts corresponding to strain variations. (**J**) Typical PL spectra taken from the WS_2 crystal on the center (C), on the body (B), and outside (A) the donut along the growth direction, revealing a bandgap shift of Δ = 90 meV, which is smaller than the 150-meV shift induced by strain-tolerant growth on 40-nm donuts.

the strain is highly localized. This curvature-induced strain was also confirmed by comparing the Raman spectra (fig. S8C), where a 1.6-cm^{-1} red shift was well resolved for the in-plane mode in the strained area.

2D crystal growth model including strain-induced nucleation site multiplication

To understand how topological strain influences growth of 2D crystals, we developed a model (see section S3 for complete description). Normal growth of the crystal is assumed to occur fairly rapidly by steps propagating along each edge once a new kink site forms, which occurs most probably at the corners of the crystal because of a lower energy barrier there, as shown in Fig. 6A. This assumption is supported by the dark stripes in the PL map (Fig. 6B) that originate from defect-induced quenching of the PL (*22*) and can be used to trace the evolution of the apexes and the origin point of the crystal nucleation. In addition, this growth process is similar to that discussed for Si/Si(111) epitaxy observed in situ by scanning tunneling microscopy (*28*).

As shown in Fig. 6A, if a step propagates with a constant velocity, v, along the crystal side, a, then the step propagation time is $\Delta t = a/v = 2H\sqrt{3}/v$. If step propagation limits the growth, then simple formulas can be derived for the outward position of a crystal facet edge, H (as defined in Fig. 6A) and its velocity, V, respectively

$$H(t) = \left(\frac{\delta v n}{\sqrt{3}} t\right)^{0.5}, V = \left(\frac{\delta v n}{\sqrt{3}}\right)^{0.5} \frac{1}{2\sqrt{t}} \quad (1)$$

where δ is the step thickness, n is the number of nucleation sites, and t is the growth time. Statistically, if the number of the nucleation sites, n, that generates the propagating steps is the same for each side, then all three sides (facets) of the crystal should grow at the same rate, producing centrosymmetric equilateral-triangle crystal shape, which is seen in image analysis in Fig. 6 (B and D) not only for both smooth substrates, but also for strain-free growth on 40-nm-deep trenches (Fig. 6, C and E).

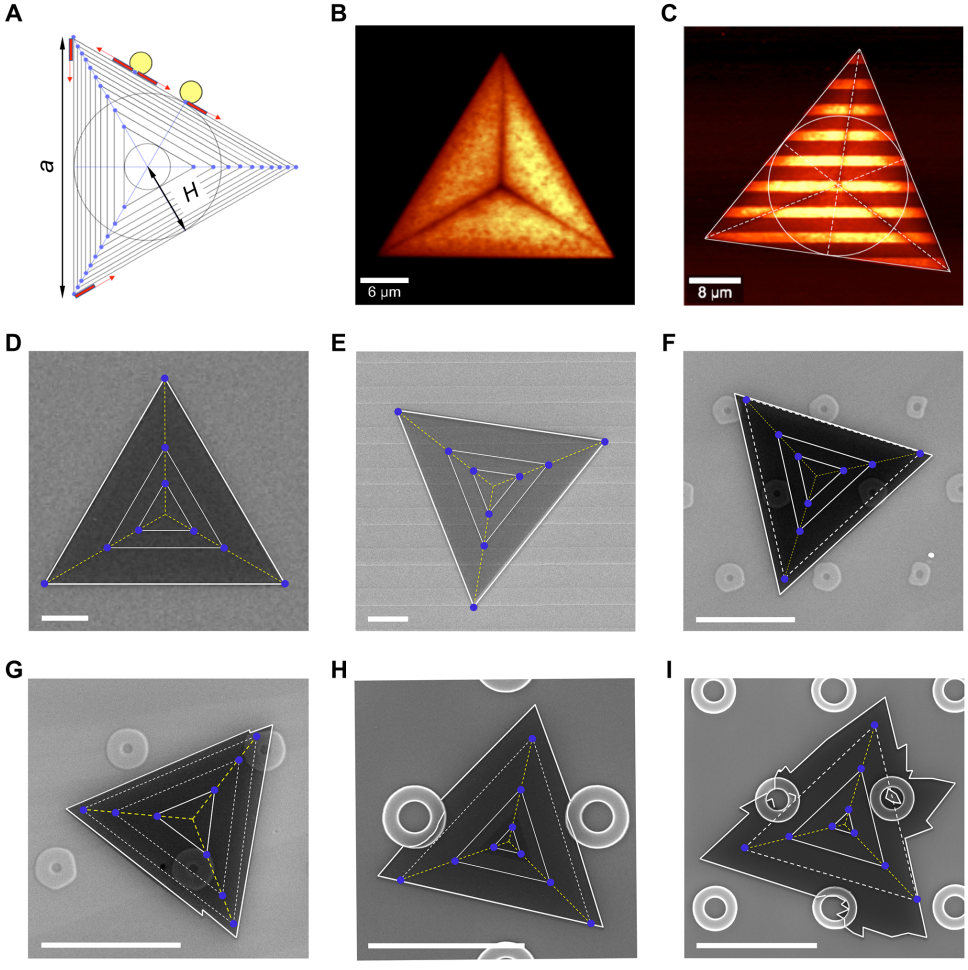

Fig. 6. Origin of asymmetric 2D crystal growth resulting from strain-induced multiplication of nucleation sites. (**A**) Illustration of the growth of a 2D crystal according to Eq. 1 when step propagation (red rectangles) from nucleation sites (blue dots) limits the crystal growth rate (see Eq. 1). The corner nucleation sites are initially responsible for a centrosymmetric growth mode. Each triangle boundary in the diagram corresponds to an additional increment in time. The yellow circles indicate obstacles such as donuts that generate additional nucleation steps (blue dots) that accelerate the growth of the affected facet, leading to noncentrosymmetric crystal growth. (**B** to **E**) Centrosymmetric growth. (**F** to **I**) Noncentrosymmetric growth. (B and C) Spatial maps of PL intensity for ML WS_2 crystals grown on a flat Si/SiO_2 substrate and on 40-nm trenches where PL minima reveal propagation of the crystal corners. (D to I) SEM images of ML grown on flat Si/SiO_2 substrates (D), 40-nm trenches (E), 40-nm donuts (F and G), and 180-nm donuts (H and I), respectively. Scale bars (in SEM images), 5 μm. Inner solid and dashed equilateral triangles in (F) to (I) are guides to assess relative facet propagation.

However, when the outward-growing crystal facet encountered a donut, a departure from centrosymmetric growth occurs. Figure 6 (F and H) shows SEM images of ML WS_2 crystals that encountered donuts on two facets. Equilateral triangles are drawn emanating from the triangle center, which was determined from PL mapping as in Fig. 6B and, in the case of Fig. 6H, a second-layer crystallite that typically nucleates in the center of the underlying crystal. As the dashed lines show in both cases, the two facets that encountered donuts have grown outward faster than the free facet. This can be understood in the frame of the model outlined above if we assume that the strain exerted by the donuts creates additional nucleation sites, as shown schematically in Fig. 6A. In this case, the number of propagating steps increases with the number of nucleation sites, n, increasing the growth rate of this specific side proportionally with the number of nucleation sites on this facet. In another case, when step nucleation limits the growth rate of a specific facet, its growth rate can be derived as

$$V = n\delta/\Delta t_{av} \quad (2)$$

where Δt_{av} is the average nucleation time of all nucleation sites at the specific crystal facet defined as $\Delta t_{av} = \sum_{i=1}^{n} \Delta t_i / n$.

Crystal branching and multiple-domain growth, as seen in Fig. 6 (G and I), are assumed to occur from the proximity of multiple additional nucleation sites generated by strain fields for a given obstacle. For example, crystal branching occurs in nearly every instance when the apex of a crystal encounters a donut. In this case, the shape of the obstacle and the location of kink nucleation sites define new growth directions. The emergence of new crystal domains is modeled in this case using a phase-field model approach (see fig. S9).

We also performed first-principles density functional theory calculations to investigate the energetics of creating edges under strain. The calculations indicate that compressive strain during growth favors more edge creation than tensile strain (see fig. S10).

DISCUSSION

The effects of topology-induced strain on the growth of 2D crystals presented here clearly indicate that Gaussian curvature can strongly affect the growth dynamics, domain morphology, and optoelectronic properties of 2D crystals, opening the door to tailored design of 2D crystals via growth on lithographically patterned substrates using curvature in the third dimension. We found three regimes, each with important technological implications. First, 2D crystals were shown to grow unhindered in rate and shape, conformally coating features with zero Gaussian curvature, even deep trenches, incurring no observable strain as measured by optical probes. This feature will allow various strategies for the vertical integration of 2D crystals, the limits of which remain to be explored. Second, a strain-tolerant growth regime was shown where 2D crystals conformed to features with Gaussian curvature, elongating and compressing to incorporate total, i.e., curvature-induced (1.1%) and global (0.4%) tensile strains up to 1.5% and highly localize bandgap shifts sufficient to shift PL peak energies of WS_2 from 1.99 to 1.82 eV, a feature that may be important for strain-induced exciton funneling. The maximum strain observed here is smaller than that predicted theoretically (8 to 11% for the features used in the study), implying that adhesion strength of the crystal to the substrate should be a key design parameter in future studies. Instead of hindering the growth, obstacles with nonzero Gaussian curvature were shown to accelerate the growth rate of particular crystal facets in the strain-tolerant regime. This growth acceleration was explained by a simple model that included strain-induced multiplication of nucleation sites induced by these obstacles. Third, growth on features with high Gaussian curvature exerted strain sufficient to break the crystal, occurring most easily at an apex of the growing triangular crystal, resulting in growth of multiple crystal domains. Intentionally exceeding the strain tolerance criteria to break 2D crystals into predictable orientations should provide a previously unknown strategy for topology-induced orientation control of patterned grains for new applications.

Conformally growing semiconducting 2D materials on lithographically prepatterned surfaces with designed positive and negative curvatures provides a new and very promising strain engineering approach for 2D materials. The previous substrate-mediated strain engineering mostly relied on the tensile or compressive strain that arose from the mismatch between the thermal coefficients of expansion of the 2D crystal and the growth substrates, which is exerted globally on all of the 2D crystals (*29*). The localized strain engineering provided by positive and negative curvatures allows one to design regions of tensile or compressive strain that can either compensate or add to the global strain exerted by the mismatch of thermal expansion coefficient with the substrate. Using current lithography and additive manufacturing at the nanoscale, this should allow the design of nanostructures and microstructures with a variety of complex positive and negative curvatures on a single wafer to produce variable optoelectronic properties through strain-tolerant growth. While stamping 2D materials onto patterned surfaces can also exert strain for bandgap tuning (*9*), wrinkles and cracks are prevalent with this technique, and great care must be taken to create sharp interfaces and minimize adsorbates. Moreover, another advantage of conformal growth compared to stamping is the demonstrated ability to coat deep trenches or features such as pits or cones (*10*). One can easily imagine 3D features (e.g., hourglass shaped) with positive and negative curvature that might be conformally coated but are impossible to stamp. In addition, intentionally designing structures that contain both strain-tolerant regions and regions to release the strain by the formation of GBs without losing conformality should allow the 3D integration of strain-engineered 2D crystals.

In summary, this novel synthetic strain engineering approach enables the conformal growth of 2D crystals on prepatterned, curved features in a scalable way, moving strain engineering of 2D materials into three dimensions, with numerous advantages over existing techniques such as stamping. The results are not only fundamentally interesting from the perspective of growth dynamics of 2D materials but also technologically important since the ability to lithographically design and synthetically engineer strain within 2D crystals on curved surfaces may enable tunable bandgaps, quantum phase transformations, and other emergent exotic properties that will be crucial for optoelectronics and other envisioned applications of 2D materials in quantum information science.

MATERIALS AND METHODS

Fabrication of patterned SiO_2/Si substrates

The fabrication of the patterned substrates was carried out using conventional contact alignment optical lithography and dry etching processes. Thermally grown SiO_2 (250 nm thick) on standard 100-mm-diameter, (100) Si wafers (University Wafer) were used. To pattern the silicon dioxide, an adhesion promoter, MicroPrime MP-P20 (Shin-Etsu MicroSi Inc.), was spin-coated at 4000 rpm, followed by the photoresist coating (MEGAPOSIT SPR955-CM 0.7, MicroChem Corp.).

Coated wafers were then soft-baked on a hot plate at 90°C for 90 s, exposed to 40 mJ/cm^2 of ultraviolet radiation using a SUSS MicroTec mask aligner, and postexposure-baked at 115°C for 90 s. The development process was carried out in a CD-26 developer (<5% tetramethylammonium hydroxide, MicroChem Corp.) for 1 min, rinsed with deionized (DI) water, and dried with nitrogen. After 1-min exposure to oxygen plasma at 100 W to remove any residual resist on the exposed area, the patterned SiO_2 was etched in an inductively coupled plasma (ICP) ion etching system (Oxford Plasmalab 100). The etch process was carried out in a mixture of 45-sccm (standard cubic centimeters per minute) SF_6 and 2-sccm O_2 at substrate temperature of 15°C. The etch depth or the height of the features was determined by the etching time. An etch time of 3 s generally resulted in an approximately 20-nm etch depth. Removal of the photoresist was carried out by exposure to oxygen plasma for 10 min, consisting of 100 sccm of oxygen at 10-W radio frequency power and 2000-W ICP power.

Growth of 2D WS_2 layered crystals by CVD

High-density WS_2 triangular crystals with a lateral length from several to hundreds of micrometers were directly grown on SiO_2/Si substrates by CVD. The details were reported in our previous publications and omitted here for brevity (*21*). Before growth, the substrates were cleaned using acetone, isopropanol, and DI water, followed by 15-min oxygen plasma treatment. To achieve clean and high-quality MLs with high yield, a seeding promoter, i.e., perylene-3,4,9,10-tetracarboxylic acid tetrapotassium salt, was spin-coated on the substrates and dried by nitrogen before loading in the CVD system (*30*).

Detaching 2D crystals from the patterned substrates and TEM sample preparation

Lift-off of WS_2 crystals from patterned substrates allow for further checking the strain and the GBs in 2D crystals directly grown on patterned substrates. First, a thin layer of poly(methyl methacrylate) (PMMA) (~180 nm, 4000 rpm, 60 s) was spun on the SiO_2/Si substrate with 2D flakes and then baked on a hot plate at 95°C for 15 min. Second, the substrate with 2D crystals was floated in KOH solvent (30 weight %, 90°C) to detach the PMMA/WS_2 thin film. Last, the thin film could be transferred onto a flat substrate, and the PMMA was then dissolved by acetone (60°C, 120 min). Note that the detachment approach described here was also used for TEM sample preparation, i.e., transfer the 2D crystals to a QUANTIFOIL TEM grid.

Morphological and structural characterizations (AFM, SEM, and STEM)

Optical images were obtained using a Nikon ECLIPSE LV100D microscope. Thickness and topographical variations of the flakes were examined with a commercial atomic force microscope (Bruker Dimension Icon) in the tapping mode. A field-emission scanning electron microscope (Zeiss Merlin) was also used to check the morphologies of the patterned features and the flakes directly grown on patterned substrates, with an operating voltage of ~10 kV. STEM imaging was carried out on a fifth-order aberration-corrected Nion UltraSTEM 100 operating at 100 kV. The STEM images were taken in the high-angle annular dark-field mode with a spatial resolution of about 1 Å.

Optical characterization by spectroscopies (Raman, PL, and SHG)

All the Raman spectra, PL spectra, and the spatial maps of Raman and PL were acquired with a laser excitation of 488 nm (2.54 eV) and recorded using a commercial system (WITec, alpha300 RA) where the laser was delivered through a single-mode optical fiber and an upright microscope using a 100× working distance objective with 0.9 NA (numeric aperture). The typical incident laser power on a sample was maintained at approximately 100 μW, while the typical acquisition times ranged from 0.05 to 0.2 s.

Some PL spectra in the Supplementary Materials were measured in a custom-built micro-PL setup. The PL was excited with a continuous wave diode-pumped solid-state laser [532 nm (2.33 eV), 100 mW; Excelsior, Spectra-Physics] through an upright microscope using a 100× working distance objective with 0.9 NA (beam spot, ~1 μm). The PL light was analyzed by a spectrometer (f = 0.3 m; SpectraPro 2300i, Acton) that was coupled to the microscope and equipped with 150, 600, and 1800 grooves/mm gratings and a charge-coupled device (CCD) camera (PIXIS: 256BR, Princeton Instruments). The typical acquisition times were varied from 0.5 to 5 s depending on the PL intensity.

SHG measurements were conducted using a 40-fs Ti:Sapphire laser (Micra, Coherent) at 800 nm and an 80-MHz repetition rate. The laser beam was passed through a half-wave plate mounted in a rotation stage and was directed into an upright microscope (Olympus) and focused onto a sample surface using a 100× microscope objective (0.9 NA) to a ~1-μm spot. The laser energy at the sample surface was ~0.1 mW. The SHG light was collected in backscattering configuration using the same objective and was directed to a monochromator (f = 0.3 m; SpectraPro 2300i, Acton) that was coupled to the microscope and equipped with a 150-grooves/mm grating and a CCD camera (PIXIS: 256BR, Princeton Instruments). Before entering the monochromator, the SHG light was passed through a short-pass cutoff filter (650 nm) and a polarizer to filter out the fundamental excitation light at 800 nm and select the SHG polarization parallel to that of the excitation light.

MD simulations

All MD simulations were performed using the large-scale atomic/molecular massively parallel simulator (LAMMPS) (*31*) simulation package and visualized using open visualization tool (OVITO) (*32*). Parameters corresponding to MoS_2 for the Stillinger-Weber potential were obtained from (*33*). Use of this potential also required making appropriate changes to one of the LAMMPS source files as described in the paper of Jiang *et al.* (*34*). The substrate in these simulations is modeled as a planar triangular lattice of particles that are displaced in the z direction that conform to a donut geometry. The interaction between the flake and the substrate particles is Lennard-Jones with parameters σ = 5.0 Å and ε = 0.1 eV. Initially, a rectangular flake consisting of two zigzag rows of MoS_2 having a width (in the x direction) of 400 Å was relaxed on the substrate. The bottom-most, the left-most, and the right-most atoms in the x direction were constrained to move in the y/z direction only. Subsequently, another zigzag row was added, and the total energy was minimized, while maintaining the same constraints. The relaxation of atoms was performed by energy minimization by first using the quickmin algorithm in LAMMPS (which essentially performs low-temperature MD) and then followed by conjugate-gradient minimization.

SUPPLEMENTARY MATERIALS

Supplementary material for this article is available at http://advances.sciencemag.org/cgi/content/full/5/5/eaav4028/DC1

Section S1. Geometrical parameters of etched patterns and continuum elasticity analysis

Section S2. Additional structural, optical characterizations, and MD simulation for asymmetric strain distribution

Section S3. Detailed analysis for the simulations of multiple domain growth

REFERENCES AND NOTES

1. J. Feng, X. Qian, C.-W. Huang, J. Li, Strain-engineered artificial atom as a broad-spectrum solar energy funnel. *Nat. Photonics* **6**, 865–871 (2012).
2. R. Roldán, A. Castellanos-Gomez, E. Cappelluti, F. Guinea, Strain engineering in semiconducting two-dimensional crystals. *J. Phys. Condens. Matter* **27**, 313201 (2015).
3. S.-W. Wang, H. Medina, K.-B. Hong, C.-C. Wu, Y. Qu, A. Manikandan, T.-Y. Su, P.-T. Lee, Z.-Q. Huang, Z. Wang, F.-C. Chuang, H.-C. Kuo, Y.-L. Chueh, Thermally strained band gap engineering of transition-metal dichalcogenide bilayers with enhanced light-matter interaction toward excellent photodetectors. *ACS Nano* **11**, 8768–8776 (2017).
4. S. Kumar, A. Kaczmarczyk, B. D. Gerardot, Strain-induced spatial and spectral isolation of quantum emitters in mono- and bilayer WSe_2. *Nano Lett.* **15**, 7567–7573 (2015).
5. A. Branny, S. Kumar, R. Proux, B. D. Gerardot, Deterministic strain-induced arrays of quantum emitters in a two-dimensional semiconductor. *Nat. Commun.* **8**, 15053 (2017).
6. A. Srivastava, M. Sidler, A. V. Allain, D. S. Lembke, A. Kis, A. Imamoğlu, Optically active quantum dots in monolayer WSe_2. *Nat. Nanotechnol.* **10**, 491–496 (2015).
7. Y. M. He, G. Clark, J. R. Schaibley, Y. He, M. C. Chen, Y. J. Wei, X. Ding, Q. Zhang, W. Yao, X. Xu, C. Y. Lu, J. W. Pan, Single quantum emitters in monolayer semiconductors. *Nat. Nanotechnol.* **10**, 497–502 (2015).
8. J.-W. Jiang, Phonon bandgap engineering of strained monolayer MoS_2. *Nanoscale* **6**, 8326–8333 (2014).
9. H. Li, A. W. Contryman, X. Qian, S. M. Ardakani, Y. Gong, X. Wang, J. W. Weisse, C. H. Lee, J. Zhao, P. M. Ajayan, J. Li, H. C. Manoharan, X. Zheng, Optoelectronic crystal of artificial atoms in strain-textured molybdenum disulphide. *Nat. Commun.* **6**, 7381 (2015).
10. H. Yu, N. Gupta, Z. Hu, K. Wang, B. R. Srijanto, K. Xiao, D. B. Geohegan, B. I. Yakobson, Tilt grain boundary topology induced by substrate topography. *ACS Nano* **11**, 8612–8618 (2017).
11. D. Sun, A. E. Nguyen, D. Barroso, X. Zhang, E. Preciado, S. Bobek, V. Klee, J. Mann, L. Bartels, Chemical vapor deposition growth of a periodic array of single-layer MoS_2 islands via lithographic patterning of an SiO_2/Si substrate. *2D Mater.* **2**, 045014 (2015).
12. C. Köhler, R. Backofen, A. Voigt, Stress induced branching of growing crystals on curved surfaces. *Phys. Rev. Lett.* **116**, 135502 (2016).
13. K. F. Mak, C. Lee, J. Hone, J. Shan, T. F. Heinz, Atomically thin MoS_2: A new direct-gap semiconductor. *Phys. Rev. Lett.* **105**, 136805 (2010).
14. S. Bertolazzi, J. Brivio, A. Kis, Stretching and breaking of ultrathin MoS_2. *ACS Nano* **5**, 9703–9709 (2011).
15. L. Mennel, M. M. Furchi, S. Wachter, M. Paur, D. K. Polyushkin, T. Muller, Optical imaging of strain in two-dimensional crystals. *Nat. Commun.* **9**, 516 (2018).
16. G. Plechinger, A. Castellanos-Gomez, M. Buscema, H. S. J. van der Zant, G. A. Steele, A. Kuc, T. Heine, C. Schüller, T. Korn, Control of biaxial strain in single-layer molybdenite using local thermal expansion of the substrate. *2D Mater.* **2**, 015006 (2015).
17. Y. Wang, C. Cong, W. Yang, J. Shang, N. Peimyoo, Y. Chen, J. Kang, J. Wang, W. Huang, T. Yu, Strain-induced direct-indirect bandgap transition and phonon modulation in monolayer WS_2. *Nano Res.* **8**, 2562–2572 (2015).
18. L. D. Landau, E. M. Lifshitz, *Theory of Elasticity, Course of Theoretical Physics* (Butterworth-Heinemann, ed. 3, 1976), vol. 7.
19. R. C. Cooper, C. Lee, C. A. Marianetti, X. Wei, J. Hone, J. W. Kysar, Nonlinear elastic behavior of two-dimensional molybdenum disulfide. *Phys. Rev. B* **87**, 35423 (2013).
20. L. Wang, A. Kutana, B. I. Yakobson, Many-body and spin-orbit effects on direct-indirect band gap transition of strained monolayer MoS_2 and WS_2. *Ann. Phys.* **526**, L7–L12 (2014).
21. K. Wang, B. Huang, M. Tian, F. Ceballos, M.-W. Lin, M. Mahjouri-Samani, A. Boulesbaa, A. A. Puretzky, C. M. Rouleau, M. Yoon, H. Zhao, K. Xiao, G. Duscher, D. B. Geohegan, Interlayer coupling in twisted WSe_2/WS_2 bilayer heterostructures revealed by optical spectroscopy. *ACS Nano* **10**, 6612–6622 (2016).
22. W. Bao, N. J. Borys, C. Ko, J. Suh, W. Fan, A. Thron, Y. Zhang, A. Buyanin, J. Zhang, S. Cabrini, P. D. Ashby, A. Weber-Bargioni, S. Tongay, S. Aloni, D. F. Ogletree, J. Wu, M. B. Salmeron, P. J. Schuck, Visualizing nanoscale excitonic relaxation properties of disordered edges and grain boundaries in monolayer molybdenum disulfide. *Nat. Commun.* **6**, 7993 (2015).
23. D.-H. Lien, J. S. Kang, M. Amani, K. Chen, M. Tosun, H.-P. Wang, T. Roy, M. S. Eggleston, M. C. Wu, M. Dubey, S.-C. Lee, J.-H. He, A. Javey, Engineering light outcoupling in 2D materials. *Nano Lett.* **15**, 1356–1361 (2015).
24. A. Berkdemir, H. R. Gutiérrez, A. R. Botello-Méndez, N. Perea-López, A. L. Elías, C.-i. Chia, B. Wang, V. H. Crespi, F. López-Urías, J.-C. Charlier, H. Terrones, M. Terrones, Identification of individual and few layers of WS_2 using Raman spectroscopy. *Sci. Rep.* **3**, 1755 (2013).
25. P. San-Jose, V. Parente, F. Guinea, R. Roldán, E. Prada, Inverse funnel effect of excitons in strained black phosphorus. *Phys. Rev. X* **6**, 031046 (2016).
26. Z. Liu, M. Amani, S. Najmaei, Q. Xu, X. Zou, W. Zhou, T. Yu, C. Qiu, A. G. Birdwell, F. J. Crowne, R. Vajtai, B. I. Yakobson, Z. Xia, M. Dubey, P. M. Ajayan, J. Lou, Strain and structure heterogeneity in MoS_2 atomic layers grown by chemical vapour deposition. *Nat. Commun.* **5**, 5246 (2014).
27. Y. Wang, V. H. Crespi, Theory of finite-length grain boundaries of controlled misfit angle in two-dimensional materials. *Nano Lett.* **17**, 5297–5303 (2017).
28. B. Voigtländer, M. Kästner, P. Smilauer, Magic islands in Si/Si(111) homoepitaxy. *Phys. Rev. Lett.* **81**, 858–861 (1998).
29. G. H. Ahn, M. Amani, H. Rasool, D.-H. Lien, J. P. Mastandrea, J. W. Ager III, M. Dubey, D. C. Chrzan, A. M. Minor, A. Javey, Strain-engineered growth of two-dimensional materials. *Nat. Commun.* **8**, 608 (2017).
30. X. Ling, Y.-H. Lee, Y. Lin, W. Fang, L. Yu, M. S. Dresselhaus, J. Kong, Role of the seeding promoter in MoS_2 growth by chemical vapor deposition. *Nano Lett.* **14**, 464–472 (2014).
31. S. Plimpton, Fast parallel algorithms for short-range molecular dynamics. *J. Comput. Phys.* **117**, 1–19 (1995).
32. A. Stukowski, Visualization and analysis of atomistic simulation data with OVITO-the Open Visualization Tool. *Model. Simul. Mater. Sci. Eng.* **18**, 015012 (2010).
33. J.-W. Jiang, H. S. Park, T. Rabczuk, Molecular dynamics simulations of single-layer molybdenum disulphide (MoS_2): Stillinger-Weber parametrization, mechanical properties, and thermal conductivity. *J. Appl. Phys.* **114**, 064307 (2013).
34. J.-W. Jiang, Z. Qi, H. S. Park, T. Rabczuk, Elastic bending modulus of single-layer molybdenum disulfide (MoS_2): Finite thickness effect. *Nanotechnology* **24**, 435705 (2013).
35. J. Bardeen, W. Shockley, Deformation potentials and mobilities in non-polar crystals. *Phys. Rev.* **80**, 72–80 (1950).
36. V. I. Artyukhov, Z. Hu, Z. Zhang, B. I. Yakobson, Topochemistry of bowtie- and star-shaped metal dichalcogenide nanoisland formation. *Nano Lett.* **16**, 3696–3702 (2016).
37. I. Steinbach, F. Pezzolla, A generalized field method for multiphase transformations using interface fields. *Physica D* **134**, 385–393 (1999).

Acknowledgments: We thank W. Liu from WITec for optical measurements. H.Y., N.G., and B.I.Y. would like to thank K. Bets for the discussions. **Funding:** The material growth and structural and optical characterizations were supported by the U.S. Department of Energy (DOE), Office of Science, Basic Energy Sciences (BES), Materials Sciences and Engineering Division and performed in part as a user project at the Center for Nanophase Materials Sciences, which is a DOE Office of Science user facility. This research used resources of the National Energy Research Scientific Computing Center (NERSC), a U.S. Department of Energy Office of Science User Facility operated under Contract No. DE-AC02-05CH11231. Work at Rice was supported by the Office of Naval Research grant N00014-18-1-2182. **Author contributions:** K.W., K.X., and D.B.G. conceived the project. K.W. and A.A.P. designed experiments. K.W., B.R.S., X.L., A.O., M.M.-S., and A.A.P. conducted and analyzed the experiments including substrate fabrication, material growth, and structural and optical characterizations. A.A.P. developed the crystal growth model, and M.Y. conducted the first-principles density functional theory calculations. H.Y., N.G., and B.I.Y. simulated the strain distribution by MD and the continuum elasticity model. Z.H. performed the phase-field simulations for crystal branching. X.G. and M.T. conducted the structure analysis by STEM. K.W., A.A.P., C.M.R., G.E., K.X., and D.B.G. wrote the manuscript. All the authors contributed to the discussion. **Competing interests:** The authors declare that they have no competing interests. **Data and materials availability:** All data needed to evaluate the conclusions in the paper are present in the paper and/or the Supplementary Materials. Additional data related to this paper may be requested from the authors.

Submitted 12 September 2018
Accepted 23 April 2019
Published 31 May 2019
10.1126/sciadv.aav4028

Citation: K. Wang, A. A. Puretzky, Z. Hu, B. R. Srijanto, X. Li, N. Gupta, H. Yu, M. Tian, M. Mahjouri-Samani, X. Gao, A. Oyedele, C. M. Rouleau, G. Eres, B. I. Yakobson, M. Yoon, K. Xiao, D. B. Geohegan, Strain tolerance of two-dimensional crystal growth on curved surfaces. *Sci. Adv.* **5**, eaav4028 (2019).